Check for updates

SOFT ROBOTS

Printing powerful soft robots on a desktop

Yichen Zhai* and Michael T. Tolley*

Copyright © 2026 The Authors, some rights reserved; exclusive licensee American Association for the Advancement of Science. No claim to original U.S. Government Works

Soft robots can achieve complex behaviors with simple control strategies. One promising approach is to embed fluidic control circuits directly into the structure of a soft robot without electronics. Automated additive manufacturing offers a route to consistently fabricate such integrated robotic systems without labor- intensive manual assembly. However, previous soft robots fabricated using this approach relied on control circuits that operated at low power, limiting their practical utility. Here, we present a 3D-printed high-power pneumatic architecture for driving soft robots. At its core is a double-expansion pneumatic oscillator inspired by the compound steam engine that converts a constant high-pressure gas input into four-phase pressure signals at high frequency. We demonstrate its use in a monolithically 3D-printed hexapod running robot capable of reaching a top speed of 4.72 meters per second with an estimated mechanical power output of 169 watts, exhibiting high-speed locomotion in a fully soft robotic system. The robot traversed rough outdoor terrain and aquatic environments and could also be operated with a liquid working medium, tap water, representing a key advance toward digitally fabricated soft robots with high performance for accomplishing real-world tasks.

INTRODUCTION

Over the past decade, researchers have developed biologically inspired soft robots with promising advantages over traditional rigid robots (*1*, *2*), including compliant interaction with the environment (*3*), adaptability (*4*), and reliable motion (*5*). To eliminate the need for electronic controllers and thereby open additional applications while reducing manufacturing cost, complementary work has demonstrated the control of soft robots with embodied physical intelligence, including mechanical or fluidic logic controllers (*6*–*10*). Electronics-free autonomous robots with embodied self-control have the potential to achieve improved operational reliability, particularly in environments where electronics may fail, while reducing reliance on complex control systems (*11*–*14*). Following this approach, we, and others, have demonstrated electronics-free soft robots that can perform tasks independently when provided with a source of pressurized air, making them suitable for real-world applications ranging from daily tasks to amphibious operation across land and water (*15*–*17*).

Despite these advantages, autonomous soft robots still face major challenges to widespread adoption, with manufacturing complexity being a major barrier. Soft robots with embodied controllers are often fabricated in multiple components through separate processes, followed by manual adjustment and assembly by skilled personnel, resulting in limited manufacturing efficiency and consistency (*10*, *11*, *18*). Recent advances have addressed this issue by demonstrating pneumatically driven autonomous robots that are operational immediately after three-dimensional (3D) printing (*19*–*22*). However, these robots still face major challenges in real applications, particularly their low power as compared with traditional rigid robotic systems. This performance gap is mainly due to the limited pressure range and corresponding flow rates of soft fluidic systems, as well as the low efficiency of converting pressurized fluid energy into mechanical work (*11*, *15*, *18*). Although several recent studies have demonstrated powerful and fast electronics-free soft locomotive robots capable of running (*23*), jumping (*24*), and flying (*25*), their control mechanisms are specific to their own geometries and cannot be directly adopted for a wide range of robotic applications. As a result, a general-purpose, high-power, and accessible fluidic control mechanism is needed for application-ready soft robots.

In this article, inspired by biological locomotion (*26*–*28*) and the compound expansion principles developed in the industrial revolution (*29*), we designed a soft, hexapod running robot (Fig. 1A) integrating a double-expansion pneumatic oscillator (Fig. 1B), which achieved fast and robust running on different terrains with a maximum speed of 4.72 m/s (Fig. 1D and movie S1). We present this work in three stages: first, a four-phase single-expansion oscillator establishing the oscillating logic; second, a double-expansion oscillator achieving increased output power and efficiency; and, last, a running robot driven by the double-expansion oscillator. In the robot, the oscillator allowed compressed air to expand twice to perform more mechanical work (Fig. 1E). The first expansion drove the inner oscillating components, and then air expanded again into the larger volume of the leg actuators for propulsion. This double-expansion mechanism allowed the oscillator to process more than 700 W of high-pressure pneumatic input power without structural failure and enabled the leg actuators to generate 169 W of mechanical output power. The oscillator itself could also be adapted to a broader range of robotic applications that require high-power cyclic pneumatic driving pressures (*30*). The running robot was designed to be 3D printed on a desktop fused filament fabrication (FFF) printer in a one-shot process without manual postassembly, enabling rapid, reproducible replication of the design. See Movie 1 for an overview of the fabrication process, operating mechanism, and experiments.

RESULTS

Four-phase single-expansion oscillator

A pneumatic circuit capable of generating outputs with four different phase offsets is required to control a legged robot with a symmetric gait (*19*). In addition, high-power locomotion further demands large airflow capacity and tolerance to high input pressures. To meet these requirements, we designed a printable bistable pneumatic comparator unit for comparing two input pressures and generating

Department of Mechanical and Aerospace Engineering, University of California San Diego, La Jolla, CA 92093, USA.
*Corresponding author. Email: zhaiyichen@ucsd.edu (Y.Z.); tolley@ucsd.edu (M.T.T.)

Downloaded from https://www.science.org on November 22, 2026

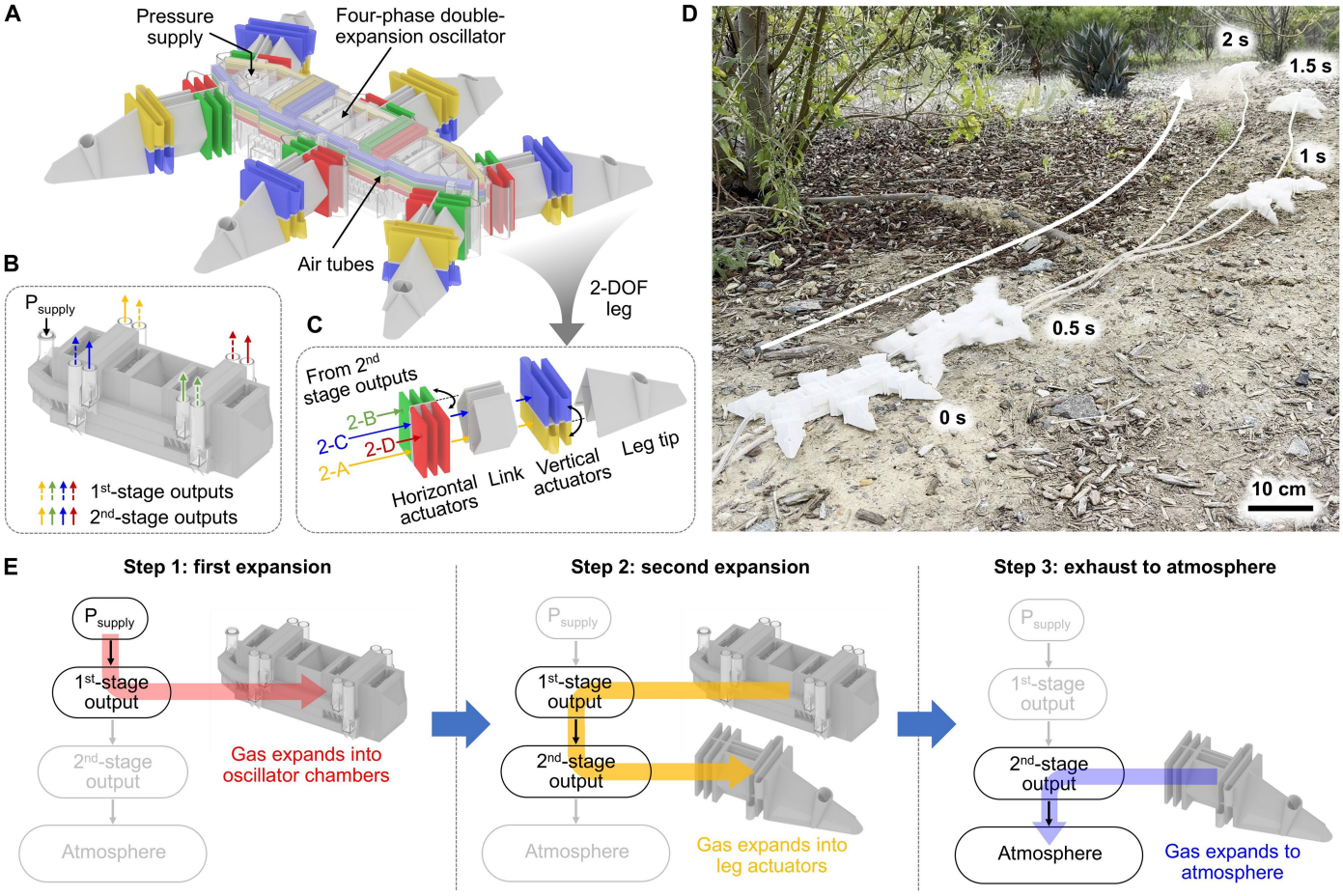
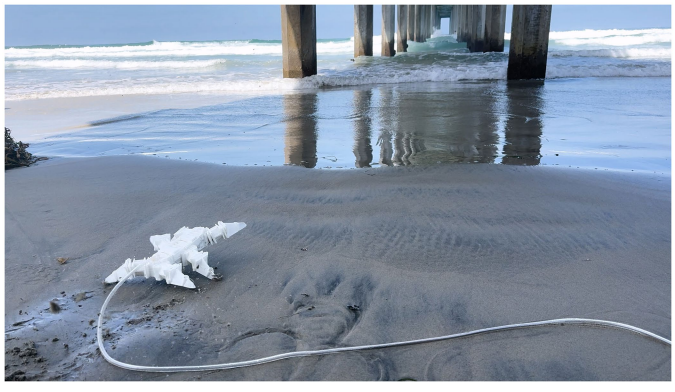


Fig. 1. Running robot powered by a double-expansion oscillator. (**A**) 3D geometry of a hexapod running robot. The four actuators on each leg are marked with four colors corresponding to the four outlets from the second stage of the double-expansion oscillator, labeled in (C). (**B**) 3D geometry of a double-expansion oscillator, showing one supply port, four first-stage output ports, and four second-stage output ports. (**C**) Disassembled view of one leg showing antagonistic pairs of lift and swing actuators driven by four second-stage outlets. (**D**) Demonstration of the robot running on an outdoor terrain. Scale bar, 10 cm. (**E**) Schematics of the airflow paths during the first expansion, second expansion, and final exhaust to the atmosphere.



Movie 1. Overview of the fabrication process, operating mechanism, and experiments of the running robot. The video clips at 0:04 to 0:11 and 0:11 to 0:18 show robots previously reported in (*6*) and (*11*), respectively.

two outputs with complementary pressures depending on the difference of the inputs (Fig. 2A). The comparator contains two opposing chambers with movable membranes, each connected to a separate beam. These beams are anchored to the outer shell by pairs of bars, whose specific lengths enforce bistability (Fig. 2D). Each bar contains two air channels connected by a vertical segment (Fig. 2B). They permit airflow in one stable state but become kinked to block airflow in the other state (Fig. 2, C and D). With appropriate external interconnections, the four channels collectively form two opposing three-port, two-position (3/2) valves (Fig. 2B), each selectively connecting an output port, either A or C, to either the pressure supply or the exhaust. Each output port is bidirectional, meaning that it can deliver pressurized air to the connected actuator during inflation and receive air back from the inflated actuator during deflation to route it to the exhaust port.

We initialized the comparator from the printed configuration (Fig. 2A) to the working configuration (Fig. 2C) by pushing either beam toward the other with an external force to kink half of the channels. The comparator could then be switched between the two states by alternately inflating the two chambers through the input ports. For example, in the state illustrated in Fig. 2C, the channels on the right side were closed, whereas the open channels on the top-left connected output A to the exhaust, and the channels on the bottom-left connected output C to the supply.

Downloaded from https://www.science.org on November 22, 2026

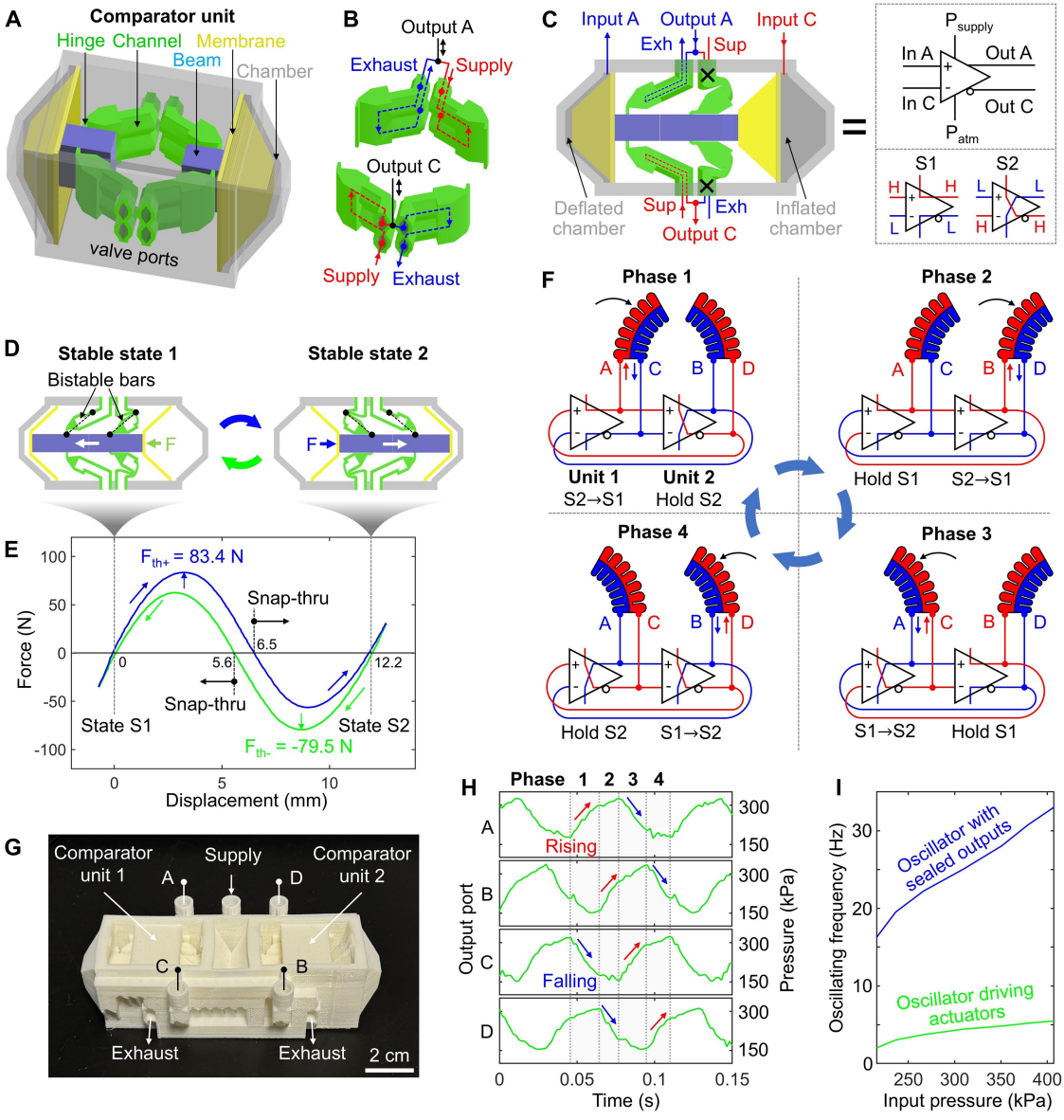


Fig. 2. A soft oscillator capable of generating four phase-offset identical oscillatory outputs. (**A**) 3D geometry of a bistable comparator unit in the original printed state. Structural supports and outer tubes are omitted. (**B**) Valve channels in a comparator showing the connections that form two three-port, two-position (3/2) valves. (**C**) Initialized comparator with beams (blue parts) in contact, showing flow paths in two opposing 3/2 valves and symbolic representation of the comparator with illustrations of two stable states, S1 and S2. H (red) and L (blue) represent high and low pressures at the input and output ports, respectively. (**D**) Cross-sectional views of the comparator showing the transition between two stable states. (**E**) Plot of the external force applied to the bistable structure of the comparator versus the resulting displacement, with the force thresholds indicated, in the absence of any pressure fluctuations in the chambers. (**F**) Symbolic schematics of the oscillating circuit, showing the states of the two comparators in each phase of one full oscillation cycle. Schematics of two antagonistic bending actuators are shown connected to the four output ports to indicate the pressure differentials during each phase. (**G**) Photograph of the oscillator, consisting of two identical comparator units with a total of four output ports, A to D. Scale bar, 2 cm. (**H**) Pressures measured experimentally at the four output ports of the oscillator running with small fixed volumes at each output port. The four phases of the system can be identified by rising edges of the four output pressures, indicated with red arrows. (**I**) Oscillating frequency versus input pressure for the oscillator with sealed outputs and when driving pneumatic actuators in a hexapod robot.

In addition to regulating airflow, the bars containing the channels, along with the central beams, formed a coupled bistable four-bar mechanism (Fig. 2D). We designed these bars with a stiffness that required a snap-through force of ~80 N (corresponding to 150 kPa applied on the membrane), as confirmed by force-displacement measurements (Fig. 2E). We chose this high force threshold to increase the pressure tolerance of the oscillator, enabling operation at much higher pressures than previously reported bistable fluidic controllers (*11*, *14*, *18*, *19*).

To analyze the propagation of logical states through fluidic control circuits, we represent the comparator symbolically with two inputs and two opposing outputs, together with its two stable states, S1 and

Downloaded from https://www.science.org on November 22, 2026

S2 (Fig. 2C). When the input pressure difference $\Delta P = P_{\text{in A}} - P_{\text{in C}}$ exceeds the increasing threshold ($\Delta P > P_{\text{th+}}$), the comparator switches to state S1, connecting out A to the supply and out C to the exhaust. When the pressure difference reverses and ΔP returns below the decreasing threshold ($\Delta P < P_{\text{th–}}$), the comparator switches to state S2 and the output connections are inverted.

To form a self-sustained oscillating circuit, we connected two or more comparators in series, with the outputs of one unit connecting to the inputs of the next and the last unit feeding back to the first to close the loop. This configuration produces a scalable oscillator architecture with any even number of symmetric phases (see Supplementary Methods). The simplest implementation is a four-phase oscillator consisting of two comparator units, whose operating sequence is illustrated in Fig. 2F (see also movie S2). To realize such an oscillator, we connected the outputs A and C of unit 1 to the inputs of unit 2, whereas the outputs B and D of unit 2 were cross-connected to the inputs of unit 1. Through their mutual coupling, the two comparators alternately triggered each other, generating an oscillation with four phases per cycle. In our printed oscillator, all four output ports remained accessible for connection to external pneumatic actuators (Fig. 2G). Pressures measured at the four ports verified the sequential pressurization of outputs A to D (Fig. 2H). The detailed mechanism is explained in Supplementary Methods.

The oscillating frequency and output power in pneumatic oscillators generally increase with supply pressure (*18*), but the maximum pressure is limited, because high pressures apply large forces that deform the soft bistable structure, eventually eliminating their bistability. By designing our four-phase oscillator with high thresholds for bistable switching, we achieved operation at input pressures up to 400 kPa resulting in oscillation frequencies exceeding 30 Hz under no-load conditions with sealed outputs. However, when pneumatic actuators were connected to the outputs, their additional volumes could reduce the frequency to 5 Hz (Fig. 2I). Moreover, directly driving a robot with this oscillator was inefficient, because high-pressure air expanded only once to inflate the actuators before being exhausted to atmosphere, leaving substantial unused energy in the exhaust flow. Because compressed air performed only a single expansion cycle in this architecture, we refer to this design as a single-expansion oscillator.

Double-expansion oscillator

Compound expansion mechanisms were widely used in early steam engines, allowing high-pressure gas to expand multiple times to convert gas energy into mechanical work (*29*). With a lower final exhaust pressure, these systems substantially enhanced overall efficiency relative to single-stage counterparts. To implement a double-expansion mechanism, we modified the comparator described above into a dual-stage design that routed the original exhaust flow into second-stage actuators to perform additional work (Fig. 3A). To achieve this, we added a third layer of channels serving as deflating channels for this extra stage. With interconnecting tubes in the outer structure, the dual-stage comparator unit had external connections for two supply ports, four output ports, and four exhaust ports (Fig. 3B). To enable additional airflow for the lower-pressure exhausts to atmosphere, we designed the deflating channels on the third layer with a larger cross-sectional area than the lower channels (12 mm^2 versus 8 mm^2, Fig. 3A). Two deflating channels on the same side were connected using an outer path, allowing simultaneous exhaust through two exhaust ports (labeled "Exh 1" or "Exh 2" in Fig. 3B).

In each of the two working states of the dual-stage comparator, half of the channels were closed (kinked), with air flowing through the open channels to inflate and deflate the actuators connected to the four output ports (Fig. 3C). The channels delivered air in two opposing flow lines (line A and line C, Fig. 3E). In each line, the four ports (supply, first-stage output, second-stage output, and exhaust) were separated by three valves arranged in series, controlling inflation, interstage equalization, and deflation. The inflating and deflating valves in the same line were always synchronized, with the interstage valve in the opposing state. In state 1, the pressure supply inflated the first-stage output 1-A through the inflating valve, and the second-stage output 2-A was deflated through the deflating valve; the air in 1-C expanded within the system to inflate 2-C through the interstage valve as the pressures in any connected volumes equalized. In state 2, all six valves were inverted: Pressures in volumes connected to 1-A and 2-A equalized, 1-C was inflated by the supply, and 2-C was deflated. The two states of the comparator with the flow paths are also represented symbolically in Fig. 3F.

To form a self-sustained double-expansion oscillator, two dual-stage comparators were interconnected through their first-stage outputs and inputs (physical realization in Fig. 3D and schematic representation in Fig. 3G). The first-stage valves and actuators resemble those of the single-expansion oscillator (Fig. 3G, components associated with ports 1-A to 1-D). Instead of being released to the atmosphere, the exhaust flow from the first-stage actuators and chambers of comparators was directed to the second-stage actuators to perform an additional expansion, which can increase the total mechanical work compared with the single-expansion oscillator (Fig. 3G, components associated with ports 2-A to 2-D). The additional work generated by the second expansion is not a fixed property of the comparator alone but depends strongly on the pressure-volume response and total volume change of the actuators connected to the second stage. If the second-stage actuators allow the partially expanded air to expand to a larger volume and a lower final pressure during each inflation, more of the remaining pneumatic energy can be converted into mechanical work. Therefore, the mechanical output efficiency is strongly affected by the exhaust pressure after each inflation. High-speed imaging confirmed that the physical realization achieved the intended two-stage expansion sequence (movie S2). With a 400-kPa supply, the oscillator produced four distinct output phases at ~30 Hz and drove four antagonistic actuators in benchtop tests (movie S2). Details of the operating sequence and experimental results are provided in Supplementary Methods.

Running robot powered by the double-expansion oscillator

To demonstrate the double-expansion oscillator in a high-power robotic system, we designed a hexapod running robot integrated with the oscillator for monolithic 3D printing (Fig. 1A and fig. S7). Actuators on different legs marked with the same color were connected to the same output port of the oscillator (Fig. 1, B and C). All actuators were connected exclusively to the second-stage low-pressure output ports, whereas the first-stage high-pressure outputs only drove the internal translation of the components in the oscillator (Fig. 1E). This configuration reduced the first-stage volume that had to be pressurized to reach the snap-through thresholds, thereby shortening the time required for the oscillator to switch and helping the robot maintain a higher stepping frequency. In addition, the leg actuators provided a much larger second-stage volume than the oscillating chambers, which was necessary for the

Downloaded from https://www.science.org on November 22, 2026

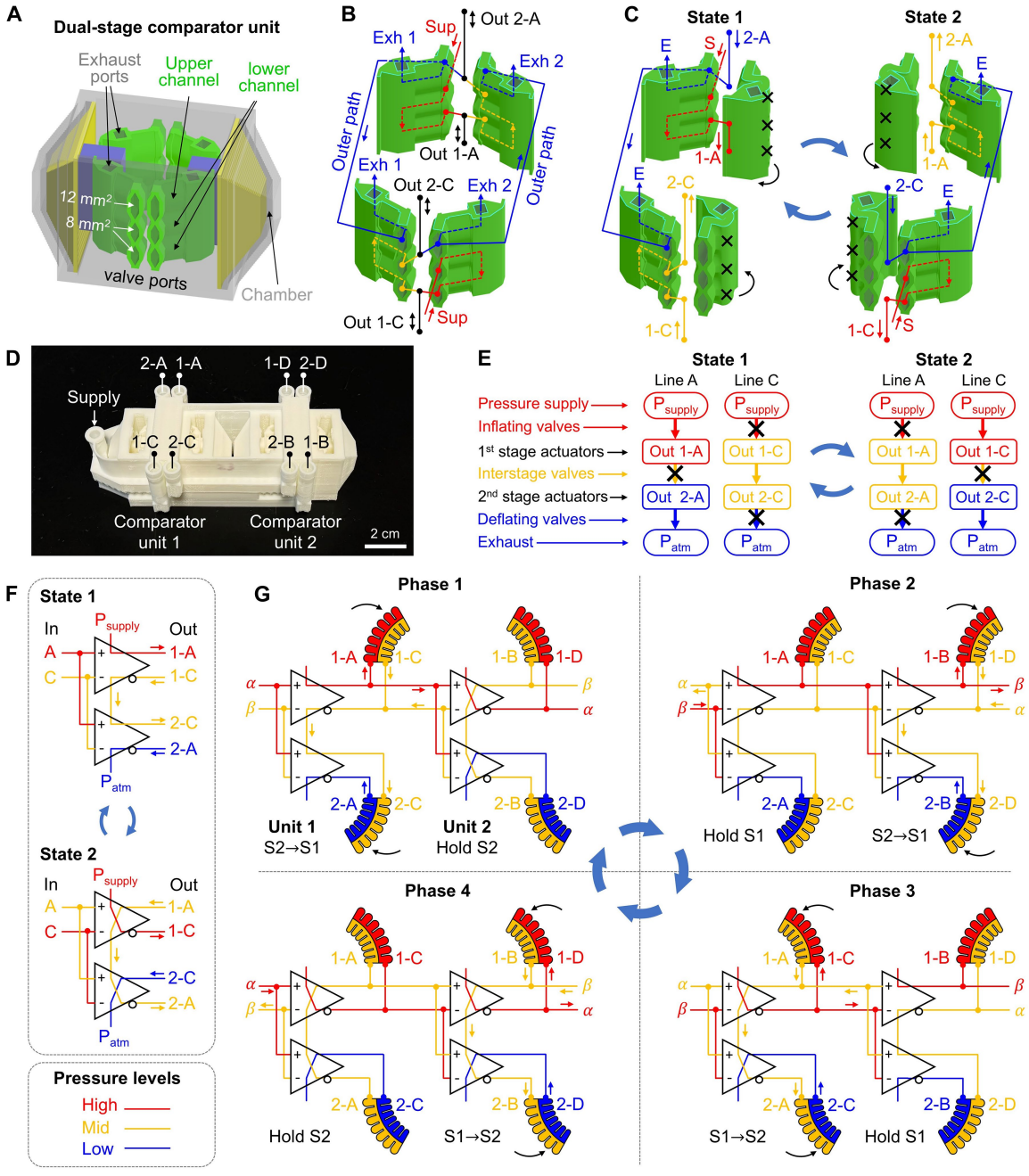


Fig. 3. Structure and mechanism of a double-expansion oscillator. (**A**) 3D geometry of a dual-stage bistable comparator unit in the original printed state. Structural supports are omitted for clarity. (**B**) Valve channels in a dual-stage comparator showing the external connections that form two compound valves with four output ports. Sup and Exh denote the supply and exhaust ports, respectively. Ports 1-A and 1-C correspond to two opposing outputs in the first stage, and ports 2-A and 2-C correspond to two opposing outputs in the second stage. (**C**) Two stable states of the channel structure, with airflow paths indicated for each state. In each state, half of the channels are closed, determining which of the outputs are being inflated, equalized, and deflated. (**D**) Photograph of the printed double-expansion oscillator, formed by two comparator units and providing eight output ports. Scale bar, 2 cm. (**E**) Airflow diagram of a comparator in its two stable states. (**F**) Symbolic representation of the dual-stage comparator illustrating the two stable states, state 1 and state 2. (**G**) Symbolic schematics of the double-expansion oscillator circuit. Four antagonistic actuators are depicted connected to the eight output ports to visually indicate the pressure changes over one oscillating cycle. Ports 1-A to 1-D are the first-stage outputs, and ports 2-A to 2-D are the second-stage outputs. Red, orange, and blue indicate high, intermediate, and low pressure levels, respectively.

Downloaded from https://www.science.org on November 22, 2026

partially expanded air to further expand and perform mechanical work efficiently.

To achieve high airtightness, the 3D geometry was designed for Eulerian-path printing (*17*), in which each layer was deposited along a continuous path without filament retraction or nozzle free motion (movie S3). The robot required no manual postassembly and became operational upon connection to a pressure supply and an initialization step using pliers (movie S4; see also Supplementary Methods). The robots were fabricated with a thermoplastic elastomer (TPE) filament. Its high elasticity, high storage modulus, and low deformation viscosity made it suitable for high-frequency repeated motion. However, variation among different filaments can affect printability and the performance of the robots, so the printing and operating settings may need to be adjusted for different filament batches (see Materials and Methods for details).

The robot was designed to execute an alternating tripod gait, in which alternating sets of three legs forming a triangle moved synchronously to propel the body forward (Fig. 4C). With a supply pressure of 408 kPa, the robot reached a stride frequency of 29 Hz. At this frequency, the four-phase actuation of each leg combined to produce an elliptical swing path in midair (Fig. 4A). On a flat surface, the running motion was captured using a high-speed camera (Fig. 4B and movie S5). In each stride cycle, the three legs of each tripod contacted the ground in phase 1 or phase 3 (respectively) and propelled the body in phase 2 or phase 4 (respectively), followed by a short aerial phase before the opposing tripod made contact. The

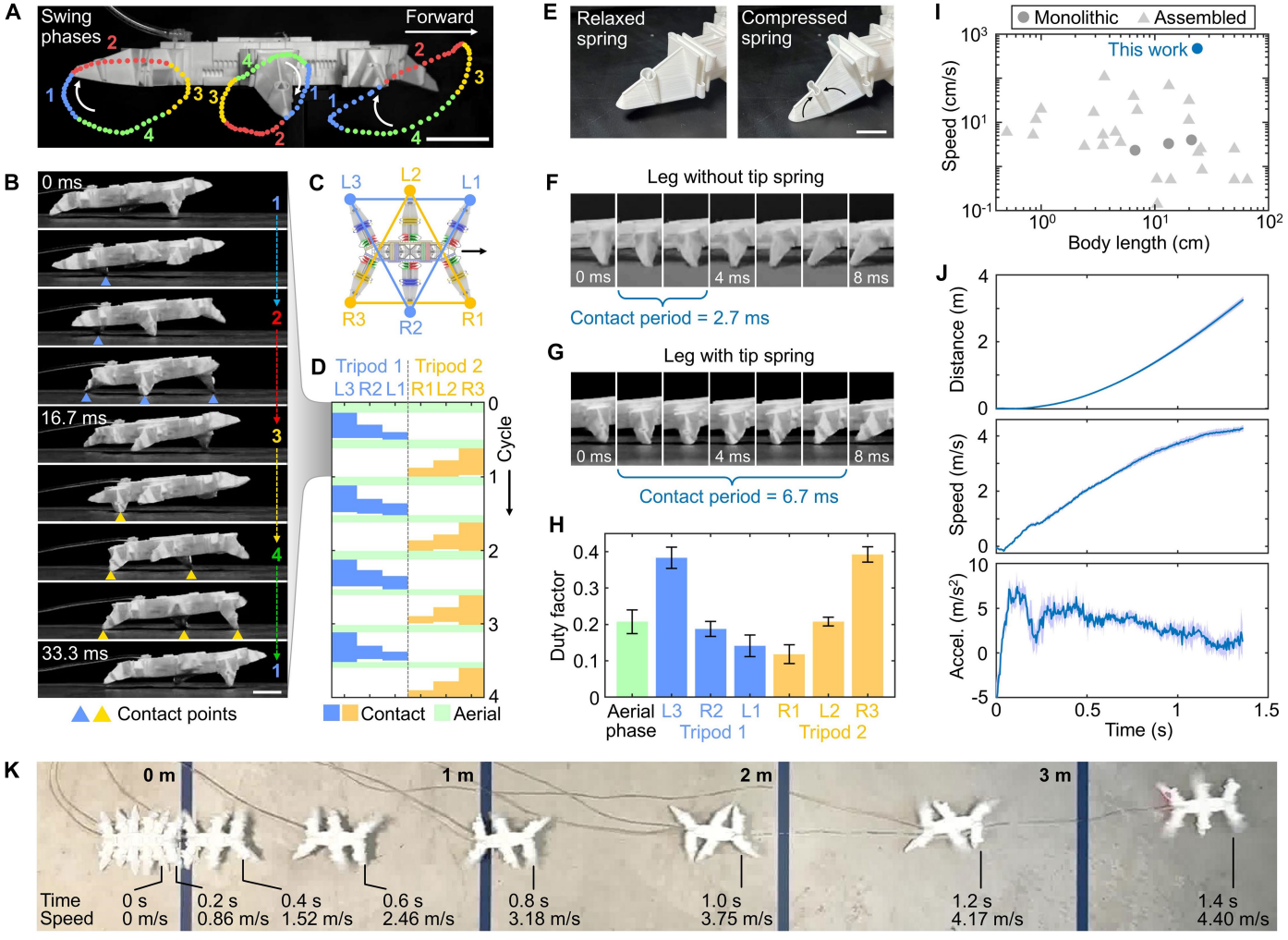


Fig. 4. Gait and speed tests of a running robot powered by a double-expansion oscillator. (**A**) Swing paths of the three right-side legs of the robot over one gait cycle, with the robot fixed in midair. (**B**) Frames from high-speed video of the robot running over one cycle, with ground contact points marked. The four phases, 1 to 4, are indicated by four colors in (A) and (B), corresponding to the phases in Fig. 3G. (**C**) Illustration of the two alternating tripods of the hexapod, with legs labeled. (**D**) Gait pattern of the robot running with an alternating tripod gait. (**E**) Improving ground contact with springs on the tips of the legs. (**F** and **G**) Frames from high-speed video showing the contact period of the right middle leg, R2, of the robot during the stance phase, for configurations without and with tip springs, respectively. (**H**) Average duty factors of the components of the running gait, including the aerial phase. Results show the average duty factors calculated from individual cycles (sample size $N = 7$), with 1 SD indicated by the error bars. (**I**) Speed versus body length of recent soft robots, categorized into monolithically fabricated and manually assembled groups. Replotted from (*23*) with additional data (see fig. S10 and table S1 for references). (**J**) Results of running tests for the robot on flat concrete, including distance, speed, and acceleration. Results show the average of five individual tests (sample size $N = 5$), with 1 SD indicated by the shaded area. (**K**) Running demonstration of the robot, with the speed indicated at each time stamp. Blue lines are spaced at 1-m intervals. Scale bars, 5 cm [(A) and (B)] and 2 cm (E).

Downloaded from https://www.science.org on November 22, 2026

gait exhibited high repeatability and robustness, with an aerial phase of ~20% of the gait cycle (Fig. 4D). The duty factors showed that the hind legs (L3 and R3) had longer contact durations than the front legs (L1 and R1) (Fig. 4H), because of a positive pitch angle induced by off-center traction forces and tether drag. Inspired by insects that use passively actuated pretarsi to stabilize ground contact (*31*), we integrated cone-shaped springs on the tips of legs to absorb impact from the rapid downward swing in phases 1 and 3 (Fig. 4E and fig. S9A). Without tip springs, the legs rebounded upon impact, resulting in short and inefficient contact periods (Fig. 4F). In contrast, a robot equipped with tip springs exhibited faster and more stable locomotion, with the contact duration increasing from 2.7 to 6.7 ms (Fig. 4G and movie S5).

Most locomotive soft robots are limited to speeds on the order of centimeters per second because of constrained actuation power (Fig. 4I), and monolithically 3D-printed robots typically fall below the average speed because of material and design limitations. In contrast, our monolithic robot achieved a peak speed of 4.72 m/s (20 BL/s) after 4 m of acceleration, demonstrating high-speed locomotion in a monolithically 3D-printed soft robotic system. Five repeated running tests on a concrete surface with a 408-kPa air supply showed highly repeatable distance, speed, and acceleration profiles over time (Fig. 4J). The instantaneous speeds at selected time points from an example test are shown in Fig. 4K.

We compared the speeds of a hexapod robot powered by a double-expansion oscillator with one powered by a single-expansion oscillator at various input pressures (Fig. 5A and movie S6). The double-expansion robot achieved substantially higher speeds across all tested pressures, indicating a higher efficiency for powering locomotion. Even with a 257-g payload (Fig. 5D and movie S7), the double-expansion robot still reached more than half of its maximum unloaded speed (2.69 m/s). Using measurements of pressure, flow rate, and volume change of actuators, we calculated the power breakdown of the double-expansion oscillator (Fig. 5A; see also Supplementary Methods), showing a maximum input power of 756 W and an estimated external mechanical power output of 169 W to the legs at a supply pressure of 415 kPa on a benchtop, with an air consumption of 254 standard liters per minute (SLPM). Internal power was consumed by driving the oscillator and inflating the tube connections, whereas exhaust power was lost in the exhaust flow. The same estimation method also showed that the single-expansion robot had a similar power output of 160 W (fig. S14A), mainly because of the overinflation of its actuators. The difference in speed was primarily caused by the much higher oscillation frequency of the

Downloaded from https://www.science.org on November 22, 2026

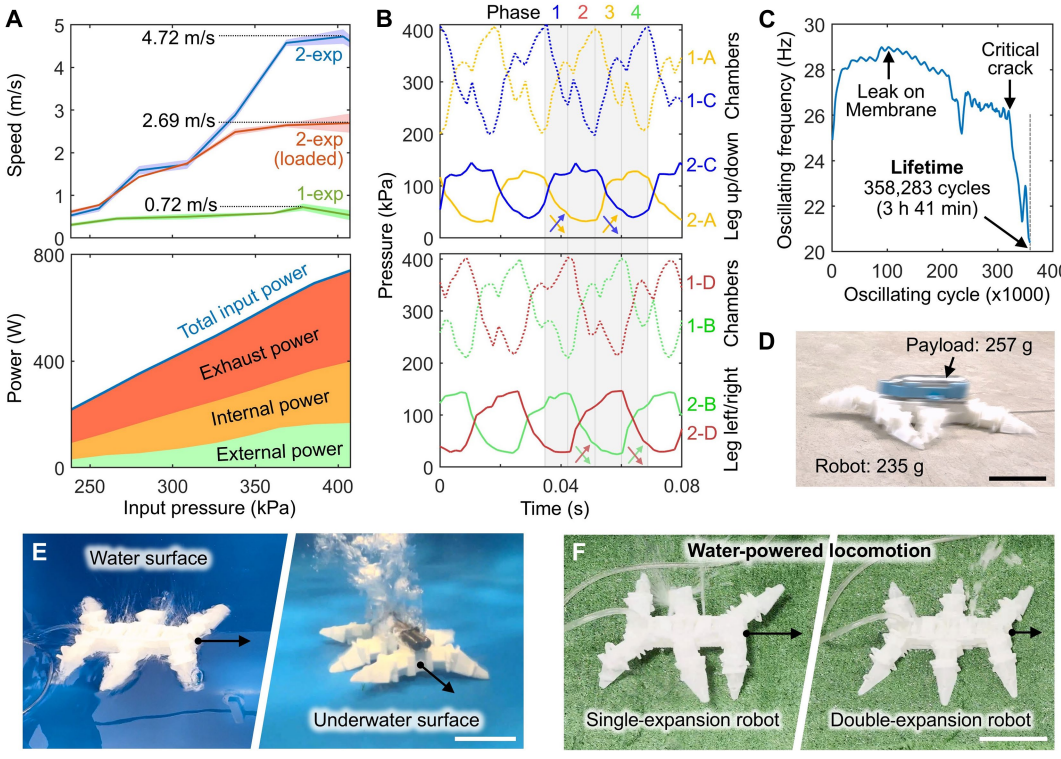


Fig. 5. Characterization and multiterrain demonstration of a running robot. (**A**) Speed and power at different input pressures. The speed comparison shows a running robot powered by a double-expansion oscillator (2-exp), in both unloaded and loaded (with a 257-g payload) configurations, and a robot powered by a single-expansion oscillator (1-exp). Results show the average of three individual tests (sample size $N = 3$), with 1 SD indicated by the shaded area. Maximum speeds are indicated for each configuration. The power breakdown shows different output components contributing to the total input power of the double-expansion running robot. (**B**) Pressures measured at the eight ports of a double-expansion oscillator embedded in a running robot. The pressures at opposing ports A and C and those at ports B and D are shown in separate plots. The four pressure phases correspond to the four swing phases in one gait cycle. (**C**) Lifetime test of the running robot showing changes in oscillating frequency versus total cycles of oscillation. (**D**) Demonstration of the running robot carrying a 257-g payload. (**E**) Demonstrations of the running robot moving on the water surface and on the underwater surface. (**F**) Demonstration of robots powered by single-expansion and double-expansion oscillators, driven by tap water at 310 kPa. Scale bars, 10 cm.

double-expansion robot, which was 5.6 times higher than that of the single-expansion robot (fig. S11E), although their stride distances were similar. As a result, the double-expansion robot achieved a 6.5-times higher maximum speed (see Supplementary Methods for details).

We measured pressures at the eight output ports of a double-expansion oscillator embedded in a running robot (Fig. 5B), with pressure phases corresponding to the leg motions in Fig. 4 (A and B). In phases 1 and 3, vertical antagonistic actuators swung because of pressure crossover between ports 2-A and 2-C, whereas in phases 2 and 4, crossover between ports 2-B and 2-D drove horizontal leg motion. Lifetime tests of five robots showed 330,000 to 380,000 oscillating cycles, corresponding to 3 to 4 hours of continuous operation before failure. An example test is shown in Fig. 5C and movie S8, illustrating the oscillation frequency over 358,283 cycles. In all tests, failure resulted from cracks propagating across the membranes under repeated oscillation (fig. S15, A and B). All cracks were located at the sharp edges of the pyramid-shaped membranes, where stress was concentrated during repeated deformation (fig. S15C). Therefore, replacing the sharp edges with rounded edges could potentially improve the durability of the robots.

The alternating tripod gait provided high ground clearance during outdoor locomotion (Fig. 1D). We tested the robot on gravel, mulch, lawn, and soil, as well as on the water surface and underwater (Fig. 5E and fig. S17). In all these tests, the robot used the same four-phase pneumatic control logic and alternating tripod gait, demonstrating that this fixed control logic could support locomotion across both terrestrial and aquatic conditions (movie S1). We measured the average moving speed in different environments (fig. S18). On outdoor terrains, the highest speed was achieved on gravel, where the robot reached 3.82 m/s. On the other terrains, because of loss of traction, the robot moved at 1.6 to 2.2 m/s. On the water surface and underwater, the robot could only move at speeds below 0.5 m/s. Further experimental details are provided in Supplementary Methods.

The high-speed running demonstration used a tethered supply to provide the required large airflow. We also tested the robot in an untethered configuration with a 16-g liquid CO_2 canister (movie S7). Because the robot consumed gas at a high flow rate of 254 SLPM and the canister stored only a limited amount of CO_2, the canister was expected to power the robot only for ~2 s. In the test, the robot showed an initial burst of motion, after which both the oscillating frequency and the speed decreased rapidly (fig. S20). The maximum speed was 1.2 m/s at 0.65 s, and the robot traveled a total distance of 1.2 m in 4.5 s. This limited performance was mainly caused by the rapid vaporization of liquid CO_2, which required heat from the ambient air, but heat transfer through the canister wall was not sufficient to sustain the required flow rate. As a result, the temperature of the canister dropped sharply, which reduced the vaporization of liquid CO_2 and lowered the output pressure and flow rate, thereby further limiting the performance of the robot. Therefore, untethered operation still requires an alternative portable pneumatic power source that can supply a higher flow rate for a longer duration, which we leave to future work.

In addition to pressurized gas, the robot could also operate when powered by tap water (Fig. 5F and movie S6). However, when we used water as the working medium, the double-expansion robot exhibited a shorter step length and lower speed than the single-expansion robot. This result shows a limitation of the double-expansion architecture. Because water is nearly incompressible, it could not provide additional expansion work in the second stage. As a result, the double-expansion robot only showed a slightly higher stepping frequency, but the volume delivered to the leg actuators came only from the limited volume decrease of the first-stage chambers during snap-through, leading to a short step length and a low moving speed. In contrast, the single-expansion robot directly pressurized the leg actuators with the supplied water, which had an effectively unlimited available volume, producing a larger step length, higher raised clearance, and higher speed. Therefore, the locomotion advantage of the double-expansion architecture mainly applies to compressible working media, such as pressurized gas. In scenarios where water is the available pressure source, the single-expansion design would be more suitable.

The robots were designed with fixed Eulerian toolpaths, in which the wall thickness was twice the printing line width. Therefore, scaling the robots required using nozzles of corresponding sizes. For example, the double-expansion running robot was originally printed using a 0.6-mm nozzle, with a length of 23.6 cm and a mass of 237 g. We printed two-thirds–scale and half-scale versions using 0.4- and 0.3-mm nozzles, respectively. The two-thirds–scale robot had a length of 15.7 cm and a mass of 73 g, whereas the half-scale robot had a length of 11.8 cm and a mass of 33 g (fig. S21). At input pressures of 430 and 272 kPa, the two-thirds–scale and half-scale robots reached speeds of 2.78 and 1.36 m/s, respectively. We demonstrated the locomotion of all three robots on a concrete surface (movie S9). Although both smaller robots reached lower maximum speeds, the two-thirds–scale robot showed higher acceleration than the full-scale robot because of its lower mass. For desktop FFF printing, the scale-up limit is mainly set by the size of the printing platform, whereas the scale-down limit is mainly set by printing defects caused by inconsistent extrusion through very small nozzles. In our tests, it was difficult to print airtight structures using nozzles smaller than 0.3 mm.

DISCUSSION

This work demonstrates that high power and fast locomotion can be achieved with fluidically powered soft robotic systems by redesigning how energy is processed and reused within fluidic control architectures. The proposed double-expansion pneumatic oscillator exploited staged expansion of the working medium, enabling substantially improved energy use while preserving the intrinsic compliance, distributed actuation, and safety of soft materials. Unlike many previously reported electronics-free oscillators that are closely tied to specific actuator geometries (*14*, *16*, *23*), this design operated as an integrated fluidic power unit intended for broad use. We demonstrated its ability to power a legged robot, and the same high-power, structured outputs are, in principle, applicable to undulatory (*32*), flapping-wing (*25*), and propulsive robots (*33*), providing an accessible route to the high-power control of soft robots.

Our running robot combined high-power output, robust multiterrain locomotion, and simple monolithic fabrication, enabling practical applications of soft robots. Its high-speed and robust locomotion across a wide range of terrains expand the application space of soft robots toward outdoor tasks traditionally dominated by rigid platforms, such as payload transport, rapid exploration, and operation on uneven or fragile surfaces. In addition, the ability to operate with different working media increases its versatility. Compressed air enabled high-speed locomotion, whereas operation powered directly by tap water allowed the use of existing water supply systems,

Downloaded from https://www.science.org on November 22, 2026

pointing to applications in irrigation systems, agricultural environments, and water-based cleaning tasks, where electrical components may be undesirable or unsafe. Moreover, the robot was produced in a single printing process using a commercial printer and material, enabling high reproducibility and minimizing the labor required for manufacturing.

The soft robot (and oscillator) still has limitations that motivate future work. The robot consumed substantial pneumatic energy and largely remained tethered to an external supply. Future designs could reduce consumption by using more efficient fluidic logic and by matching the oscillator's output pressure and volume more closely to the requirements of the actuators. For applications with lower performance requirements, the robot could be powered by portable pressure sources and thus move over longer distances instead of remaining near a stationary supply of pressurized fluid. In addition, embedding fluidic intelligence for sensing (*34*), simple decision-making (*35*), sequencing (*36*), and steering (*37*) will be needed to produce complex behaviors and task-level control without electronics. Extending the same design principles to systems that perform manipulation, coordinated motion, and repeated actions could lead to soft platforms suitable for additional applications, including both field tasks and automated production environments.

MATERIALS AND METHODS

Generation of Eulerian path for printing

The design method for monolithic printed robots with Eulerian paths was described in our previous work (*17*). We applied three rules to the original computer-aided design (CAD) geometries of the oscillators and running robots in this work. First, all vertical walls were designed with a thickness of 0.9 mm. Second, all independent components (mostly the vertical actuators of the legs) were connected into a single component with 0.9-mm-wide deformable bridges, which allowed relative movement between components. Last, for structures with local closed-loop geometries, a 0.04-mm gap was added to cut each loop and generate a single path. We then sliced the CAD geometries with commercial slicer software (ideaMaker, Raise3D Technologies) to generate the printing toolpaths. With these three rules, we only needed to set the printing line width to 0.45 mm in the slicer, and continuous Eulerian paths were generated automatically for all layers.

Modifications to the 3D printer

We printed all devices in this work on a commercially available desktop 3D printer (Raise3D E2, Raise3D Technologies) after modifying the control system, nozzle, and cooling components. We disconnected the built-in user-interface computer and connected a laptop running commercial monitoring software (Repetier-Server, Hot-World) to the motion control board by a universal serial bus (USB) cable. The modifications to the hardware are shown in fig. S22. We replaced the original nozzle with a 0.6-mm brass nozzle and set the line width in the slicer to 0.45 mm to apply a 25% overlap between adjacent lines. To enhance cooling, we replaced the original part-cooling fan on the print head with a blowing system using compressed air. We used a digital proportional pressure regulator (VPPI-5L-3-G18-0L10H-V1-S1D, Festo) to provide pressurized air to a customized 3D-printed blower for part cooling. The original pulse-width-modulation control signal on the motion board for the cooling fan was rewired to the input port of the proportional pressure regulator, to adjust its output pressure directly on the basis of the G-code. The maximum output pressure of the regulator was set to 35 psi (241 kPa), which corresponded to an airflow of 140 SLPM. We coated the heating block of the nozzle with silicone glue to maintain its temperature under the high airflow.

Monolithic fabrication and initialization of the robots

The 3D CAD design files of the oscillators and running robots are provided in data file S2. The parameters used for printing are listed in table S2. The printing material was 83A TPE filament (3DNE0017510, NinjaTek). We found that the TPE filament purchased before April 2025 with lot numbers up to 769564 was more suitable for printing these designs and produced fewer defects. When printing with filament from later lot numbers, the printing speed had to be reduced from 30 to 20 mm/s to allow a longer cooling time for successfully building the structures. Also, the supplied pressure for operating the robots needed to be reduced by 50 to 100 kPa because of the lower stiffness of the newer material. The printing process was fully monolithic and did not require manual assembly. After printing, we sprayed ethanol on the printing platform and used a paint scraper to separate the printed workpieces from the platform (movie S4). The printed robots were manually initialized from the printed configuration to the working configuration using the method described in Supplementary Methods. We used sharp-nose pliers to push one of the two beams in each comparator to the opposite side for initialization. After initialization, the robots became operational immediately once a pressure supply was connected. However, the running speed of a newly printed robot is typically half of its maximum value. To reach the maximum speed, the robot needs to oscillate in midair at a high input pressure (300 to 400 kPa) for at least 10 min to relieve the initial stress in the TPE material, as indicated by the increasing oscillating frequency during the first 20,000 cycles of the lifetime test (Fig. 5C).

Indoor tests of the running robot

In the indoor tests, we used a digital proportional pressure regulator (VPPI-5L-3-G18-0L10H-V1-S1D, Festo) to regulate the laboratory compressed-air supply at 135 psi (930 kPa) to the desired pressures and deliver air to the running robot through a 7-m tube [3.18 mm inner diameter (ID) by 6.35 mm outer diameter (OD), Tygon]. The real-time speed of the robot (Fig. 4, J and K) was extracted from slow-motion videos recorded at 240 frames per second (fps) by a cellphone mounted 3 m above the ground. The top speeds at different supply pressures (Fig. 5A) were measured with the setup shown in fig. S23. Two parallel laser beams with a 60-cm spacing were generated by laser diodes and oriented perpendicular to the robot's runway. Two phototransistors (Laser Sensor Module, Acxico) were placed on the opposite side to detect the laser signals. We calculated the speed of the robot from the time difference between the moments when the robot blocked each laser beam. The robot was initially placed 4 m away from the first laser beam so that it could accelerate to its maximum speed.

Outdoor tests of the running robot

In the outdoor and aquatic tests, we used an air compressor (DWFP-55126, DeWalt) to supply airflow through a 4.5-m tube (3.18 mm ID by 6.35 mm OD, Tygon). The setup is shown in fig. S16. The output pressure was set to the maximum range (~1000 kPa), with the flow rate limited to 160 SLPM by the compressor. For the test on the

Downloaded from https://www.science.org on November 22, 2026

water surface, the robot was modified to increase its buoyancy (Supplementary Methods). In the underwater test, a 447-g payload was fixed to the robot to sink it to the bottom. In the water-driven tests, we used a 4-m tube (4.76 mm ID by 9.68 mm OD, Tygon) to connect the robots directly to the tap water supply at a pressure of 310 kPa.

Force measurements

We prepared a comparator unit for testing and mounted it on a force tester (ESM750S, Mark-10) with a 100-N force gauge (Series 7, Mark-10) to measure the bistable force as a function of displacement. Two 3D-printed rigid holders were attached to the shell and the membranes of the comparator unit, respectively (fig. S9C). The comparison of forces on leg tips with and without a spring was also measured using the same force tester (fig. S9B). The tips were mounted on the force gauge with a 38° downward pitch angle, corresponding to the maximum downward bending angle during the vertical swing phase.

Pressure and flow rate measurements

The real-time output pressures of the oscillator and the running robot were measured using four 100-psi (689-kPa) pressure sensors (SSCDANN100PGAA5, Honeywell) with an Arduino-based readout. The setup for pressure measurements is shown in fig. S11F. A MATLAB program was used to control the digital proportional pressure regulator and to collect pressure data from the Arduino. The pressure was supplied from the regulator to the robot through a 7-m tube, which introduced a substantial pressure drop along the tube. The input pressures shown in Fig. 5A were average pressures measured at the input port of the robot. The relationship between the pressure setting at the regulator and the input pressure at the robot is shown in fig. S11A. All flow rates in this work were measured with a mass flow meter (FMA-1611A-V2, Omega).

High-speed video recordings

We used a high-speed camera (VEO 410L, Phantom) with micro lenses (24 to 85 mm f/2.8–4D, Nikon) to capture the motion of the oscillators and the running robot. Videos of the oscillators were recorded at 3500 fps, and side-view videos of the robot running on the surface were recorded at 1500 fps. The resolution of the recorded videos was 1280 pixels by 800 pixels.

Statistical analysis

Experimental data in Figs. 4 (H and J) and 5A are presented as mean values ± 1 SD indicated by error bars or shaded areas. The number of measurements or repeated tests (sample size) is indicated in the corresponding figure captions. No statistical significance tests were performed in this work.

Supplementary Materials

The PDF file includes:
Methods
Figs. S1 to S23
Tables S1 and S2
Legends for movies S1 to S9
References (*38*–*55*)

Other Supplementary Material for this manuscript includes the following:
Movies S1 to S9
Data files S1 and S2

REFERENCES AND NOTES

1. F. Ilievski, A. D. Mazzeo, R. F. Shepherd, X. Chen, G. M. Whitesides, Soft robotics for chemists. *Angew. Chem. Int. Ed. Engl.* **50**, 1890–1895 (2011).
2. D. Rus, M. T. Tolley, Design, fabrication and control of soft robots. *Nature* **521**, 467–475 (2015).
3. T. J. K. Buchner, S. Rogler, S. Weirich, Y. Armati, B. G. Cangan, J. Ramos, S. T. Twiddy, D. M. Marini, A. Weber, D. Chen, G. Ellson, J. Jacob, W. Zengerle, D. Katalichenko, C. Keny, W. Matusik, R. K. Katzschmann, Vision-controlled jetting for composite systems and robots. *Nature* **623**, 522–530 (2023).
4. C. Laschi, B. Mazzolai, M. Cianchetti, Soft robotics: Technologies and systems pushing the boundaries of robot abilities. *Sci. Robot.* **1**, eaah3690 (2016).
5. R. F. Shepherd, F. Ilievski, W. Choi, S. A. Morin, A. A. Stokes, A. D. Mazzeo, X. Chen, M. Wang, G. M. Whitesides, Multigait soft robot. *Proc. Natl. Acad. Sci. U.S.A.* **108**, 20400–20403 (2011).
6. M. T. Tolley, R. F. Shepherd, B. Mosadegh, K. C. Galloway, M. Wehner, M. Karpelson, R. J. Wood, G. M. Whitesides, A resilient, untethered soft robot. *Soft Robot.* **1**, 213–223 (2014).
7. C. Laschi, B. Mazzolai, V. Mattoli, M. Cianchetti, P. Dario, Design of a biomimetic robotic octopus arm. *Bioinspir. Biomim.* **4**, 015006 (2009).
8. C. D. Onal, D. Rus, Autonomous undulatory serpentine locomotion utilizing body dynamics of a fluidic soft robot. *Bioinspir. Biomim.* **8**, 026003 (2013).
9. P. Rothemund, A. Ainla, L. Belding, D. J. Preston, S. Kurihara, Z. Suo, G. M. Whitesides, A soft, bistable valve for autonomous control of soft actuators. *Sci. Robot.* **3**, eaar7986 (2018).
10. M. Wehner, R. L. Truby, D. J. Fitzgerald, B. Mosadegh, G. M. Whitesides, J. A. Lewis, R. J. Wood, An integrated design and fabrication strategy for entirely soft, autonomous robots. *Nature* **536**, 451–455 (2016).
11. D. Drotman, S. Jadhav, D. Sharp, C. Chan, M. T. Tolley, Electronics-free pneumatic circuits for controlling soft-legged robots. *Sci. Robot.* **6**, eaay2627 (2021).
12. J. D. Hubbard, R. Acevedo, K. M. Edwards, A. T. Alsharhan, Z. Wen, J. Landry, K. Wang, S. Schaffer, R. D. Sochol, Fully 3D-printed soft robots with integrated fluidic circuitry. *Sci. Adv.* **7**, eabe5257 (2021).
13. L. C. van Laake, J. de Vries, S. Malek Kani, J. T. B. Overvelde, A fluidic relaxation oscillator for reprogrammable sequential actuation in soft robots. *Matter* **5**, 2898–2917 (2022).
14. W. K. Lee, D. J. Preston, M. P. Nemitz, A. Nagarkar, A. K. MacKeith, B. Gorissen, N. Vasios, V. Sanchez, K. Bertoldi, L. Mahadevan, G. M. Whitesides, A buckling-sheet ring oscillator for electronics-free, multimodal locomotion. *Sci. Robot.* **7**, eabg5812 (2022).
15. D. J. Preston, P. Rothemund, H. J. Jiang, M. P. Nemitz, J. Rawson, Z. Suo, G. M. Whitesides, Digital logic for soft devices. *Proc. Natl. Acad. Sci. U.S.A.* **116**, 7750–7759 (2019).
16. C. J. Decker, H. J. Jiang, M. P. Nemitz, S. E. Root, A. Rajappan, J. T. Alvarez, J. Tracz, L. Wille, D. J. Preston, G. M. Whitesides, Programmable soft valves for digital and analog control. *Proc. Natl. Acad. Sci. U.S.A.* **119**, e2117469119 (2022).
17. Y. Zhai, A. De Boer, J. Yan, B. Shih, M. Faber, J. Speros, R. Gupta, M. T. Tolley, Desktop fabrication of monolithic soft robotic devices with embedded fluidic control circuits. *Sci. Robot.* **8**, eadg3792 (2023).
18. D. J. Preston, H. J. Jiang, V. Sanchez, P. Rothemund, J. Rawson, M. P. Nemitz, W. K. Lee, Z. Suo, C. J. Walsh, G. M. Whitesides, A soft ring oscillator. *Sci. Robot.* **4**, eaaw2344 (2019).
19. Y. Zhai, J. Yan, A. De Boer, M. Faber, R. Gupta, M. T. Tolley, Monolithic desktop digital fabrication of autonomous walking robots. *Adv. Intell. Syst.* **7**, 2400025 (2025).
20. Y. Zhai, M. T. Tolley, Electronics-free 3D-printed soft swimming robot with pneumatic oscillating control for efficient undulating locomotion. *IEEE Robot. Autom. Lett.* **10**, 7891–7898 (2025).
21. M. Gepner, J. Mack, A. A. Stokes, A standardized platform for translational advances in fluidic soft systems. *Device* **3**, 100800 (2025).
22. S. Conrad, J. Teichmann, P. Auth, N. Knorr, K. Ulrich, D. Bellin, T. Speck, F. J. Tauber, 3D-printed digital pneumatic logic for the control of soft robotic actuators. *Sci. Robot.* **9**, eadh4060 (2024).
23. A. Comoretto, H. A. H. Schomaker, J. T. B. Overvelde, Physical synchronization of soft self-oscillating limbs for fast and autonomous locomotion. *Science* **388**, 610–615 (2025).
24. G. Chen, Y. Long, S. Yao, S. Tang, J. Luo, H. Wang, Z. Zhang, H. Jiang, A non-electrical pneumatic hybrid oscillator for high-frequency multimodal robotic locomotion. *Nat. Commun.* **16**, 1234 (2025).
25. Y. Zhao, Y. Qi, J. Shao, B. Sun, M. Wang, S. Zhong, Y. Yang, An energy-efficient and powerful oscillator for micro-air vehicles with electronics-free flapping. *IEEE Robot. Autom. Lett.* **11**, 3174–3181 (2026).
26. P. Holmes, R. J. Full, D. Koditschek, J. Guckenheimer, The dynamics of legged locomotion: Models, analyses, and challenges. *SIAM Rev.* **48**, 207–304 (2006).
27. P. Ramdya, R. Thandiackal, R. Cherney, T. Asselborn, R. Benton, A. J. Ijspeert, D. Floreano, Climbing favours the tripod gait over alternative faster insect gaits. *Nat. Commun.* **8**, 14494 (2017).

Downloaded from https://www.science.org on November 22, 2026

28. T. Weihmann, P. G. Brun, E. Pycroft, Speed dependent phase shifts and gait changes in cockroaches running on substrates of different slipperiness. *Front. Zool.* **14**, 24 (2017).
29. J. T. Van Riemsdijk, The compound locomotive, part I, 1876 to 1901. *Trans. Newcomen Soc.* **43**, 1–17 (1970).
30. P. Polygerinos, N. Correll, S. A. Morin, B. Mosadegh, C. D. Onal, K. Petersen, M. Cianchetti, M. T. Tolley, R. F. Shepherd, Soft robotics: Review of fluid-driven intrinsically soft devices; manufacturing, sensing, control, and applications in human-robot interaction. *Adv. Eng. Mater.* **19**, 1700016 (2017).
31. W. Federle, E. L. Brainerd, T. A. McMahon, B. Hölldobler, Biomechanics of the movable pretarsal adhesive organ in ants and bees. *Proc. Natl. Acad. Sci. U.S.A.* **98**, 6215–6220 (2001).
32. R. K. Katzschmann, J. DelPreto, R. MacCurdy, D. Rus, Exploration of underwater life with an acoustically controlled soft robotic fish. *Sci. Robot.* **3**, eaar3449 (2018).
33. C. Christianson, Y. Cui, M. Ishida, X. Bi, Q. Zhu, G. Pawlak, M. T. Tolley, Cephalopod-inspired robot capable of cyclic jet propulsion through shape change. *Bioinspir. Biomim.* **16**, 016014 (2020).
34. C. Hegde, J. Su, J. M. R. Tan, K. He, X. Chen, S. Magdassi, Sensing in soft robotics. *ACS Nano* **17**, 15277–15307 (2023).
35. S. Picella, C. M. van Riet, J. T. B. Overvelde, Pneumatic coding blocks enable programmability of electronics-free fluidic soft robots. *Sci. Adv.* **10**, eadr2433 (2024).
36. A. A. Stanley, E. S. Roby, S. J. Keller, High-speed fluidic processing circuits for dynamic control of haptic and robotic systems. *Sci. Adv.* **10**, eadl3014 (2024).
37. A. Comoretto, S. Koppen, T. Mandke, J. T. B. Overvelde, Embodying mechano-fluidic memory in soft machines to program behaviors upon interactions. *Device* **3**, 100863 (2025).
38. M. Cai, K. Kawashima, T. Kagawa, Power assessment of flowing compressed air. *J. Fluids Eng. Trans. ASME* **128**, 402–405 (2006).
39. A. Aubin, R. H. Heisser, O. Peretz, J. Timko, J. Lo, E. F. Helbling, S. Sobhani, A. D. Gat, R. F. Shepherd, Powerful, soft combustion actuators for insect-scale robots. *Science* **381**, 1212–1217 (2023).
40. R. Chen, Z. Yuan, J. Guo, L. Bai, X. Zhu, F. Liu, H. Pu, L. Xin, Y. Peng, J. Luo, L. Wen, Y. Sun, Legless soft robots capable of rapid, continuous, and steered jumping. *Nat. Commun.* **12**, 7028 (2021).
41. Z. Xiong, Y. Su, H. Lipson, "Fast untethered soft robotic crawler with elastic instability" in *Proceedings of the IEEE International Conference on Robotics and Automation* (IEEE, 2023), pp. 1613–1619.
42. Y. Wu, J. K. Yim, J. Liang, Z. Shao, M. Qi, J. Zhong, Z. Luo, X. Yan, M. Zhang, X. Wang, R. S. Fearing, R. J. Full, L. Lin, Insect-scale fast moving and ultrarobust soft robot. *Sci. Robot.* **4**, eaax1594 (2019).
43. Y. Tang, Y. Chi, J. Sun, T. H. Huang, O. H. Maghsoudi, A. Spence, J. Zhao, H. Su, J. Yin, Leveraging elastic instabilities for amplified performance: Spine-inspired high-speed and high-force soft robots. *Sci. Adv.* **6**, eaaz6912 (2020).
44. G. Mao, D. Schiller, D. Danninger, B. Hailegnaw, F. Hartmann, T. Stockinger, M. Drack, N. Arnold, M. Kaltenbrunner, Ultrafast small-scale soft electromagnetic robots. *Nat. Commun.* **13**, 4453 (2022).
45. T. Umedachi, V. Vikas, B. A. Trimmer, Softworms: The design and control of non-pneumatic, 3D-printed, deformable robots. *Bioinspir. Biomim.* **11**, 025007 (2016).
46. W. Hu, G. Z. Lum, M. Mastrangeli, M. Sitti, Small-scale soft-bodied robot with multimodal locomotion. *Nature* **554**, 81–85 (2018).
47. M. A. Robertson, J. Paik, New soft robots really suck: Vacuum-powered systems empower diverse capabilities. *Sci. Robot.* **2**, eaan6357 (2017).
48. X. Huang, K. Kumar, M. K. Jawed, A. M. Nasab, Z. Ye, W. Shan, C. Majidi, Chasing biomimetic locomotion speeds: Creating untethered soft robots with shape memory alloy actuators. *Sci. Robot.* **3**, eaau7557 (2018).
49. J. Zhao, J. Zhang, D. McCoul, Z. Hao, S. Wang, X. Wang, B. Huang, L. Sun, Soft and fast hopping-running robot with speed of six times its body length per second. *Soft Robot.* **6**, 114–124 (2019).
50. T. Park, Y. Cha, Soft mobile robot inspired by animal-like running motion. *Sci. Rep.* **9**, 14011 (2019).
51. X. Ji, X. Liu, V. Cacucciolo, M. Imboden, Y. Civet, A. El Haitami, S. Cantin, Y. Perriard, H. Shea, An autonomous untethered fast soft robotic insect driven by low-voltage dielectric elastomer actuators. *Sci. Robot.* **4**, eaaz6451 (2019).
52. J. Liang, Y. Wu, J. K. Yim, H. Chen, Z. Miao, H. Liu, Y. Liu, Y. Liu, D. Wang, W. Qiu, Z. Shao, M. Zhang, X. Wang, J. Zhong, L. Lin, Electrostatic footpads enable agile insect-scale soft robots with trajectory control. *Sci. Robot.* **6**, eabe7906 (2021).
53. B. Gorissen, E. Milana, A. Baeyens, E. Broeders, J. Christiaens, K. Collin, D. Reynaerts, M. De Volder, Hardware sequencing of inflatable nonlinear actuators for autonomous soft robots. *Adv. Mater.* **31**, e1804598 (2019).
54. H. Tsukagoshi, A. Kitagawa, K. Tambo, H. Chiba, "A fluid self-excited oscillation peculiar to flat ring tube and its application to wearable robots" in *Proceedings of the IEEE International Conference on Robotics and Automation* (IEEE, 2007), pp. 266–271.
55. L. Zhao, Y. Jiang, M. Chen, K. Bekris, D. Balkcom, Modular shape-changing tensegrity-blocks enable self-assembling robotic structures. *Nat. Commun.* **16**, 88 (2025).

Acknowledgments: We thank J. Yan for assistance with video recording during the outdoor tests and during the operation of the robot after monolithic printing. **Funding:** This work was supported by the National Science Foundation through the Foundational Research in Robotics (FRR) program (grant no. 2331917). **Author contributions:** Y.Z. and M.T.T. conceived the project. Y.Z. designed the study, developed the methods and experimental setups, performed the experiments, and analyzed the data. Y.Z. wrote the initial manuscript. Y.Z. and M.T.T. discussed the results and revised the manuscript. M.T.T. secured funding and supervised the research. **Competing interests:** Y.Z. and M.T.T. are inventors on a US provisional patent application related to the work described in this article. The authors declare that they have no other competing interests. **Data, code, and materials availability:** All data and materials needed to reproduce the results of this study are available in the article, the Supplementary Materials, and the Dryad repository (doi:10.5061/dryad.sxksn03m0).

Submitted 16 April 2026
Accepted 21 October 2026
Published 18 November 2026
10.1126/scirobotics.aei1264

Downloaded from https://www.science.org on November 22, 2026

Science Robotics

Printing powerful soft robots on a desktop

Yichen Zhai and Michael T. Tolley

Sci. Robot. **11** (120), eaei1264. DOI: 10.1126/scirobotics.aei1264

View the article online
https://www.science.org/doi/10.1126/scirobotics.aei1264
Permissions
https://www.science.org/help/reprints-and-permissions

Downloaded from https://www.science.org on November 22, 2026

Use of this article is subject to the Terms of service

Science Robotics (ISSN 2470-9476) is published by the American Association for the Advancement of Science. 1200 New York Avenue NW, Washington, DC 20005. The title *Science Robotics* is a registered trademark of AAAS.

Copyright © 2026 The Authors, some rights reserved; exclusive licensee American Association for the Advancement of Science. No claim to original U.S. Government Works